micromachines

MDPI

Article

Photogating Effect of Atomically Thin Graphene/MoS_2/$MoTe_2$ van der Waals Heterostructures

Do-Hyun Park [1] and Hyo Chan Lee [2,*]

[1] Division of Quantum Phase and Devices, Konkuk University, Seoul 05029, Republic of Korea
[2] Chemical Engineering, Myongji University, Yongin 17058, Republic of Korea
* Correspondence: hyochan@mju.ac.kr

Abstract: The development of short-wave infrared photodetectors based on various two-dimensional (2D) materials has recently attracted attention because of the ability of these devices to operate at room temperature. Although van der Waals heterostructures of 2D materials with type-II band alignment have significant potential for use in short-wave infrared photodetectors, there is a need to develop photodetectors with high photoresponsivity. In this study, we investigated the photogating of graphene using a monolayer-MoS_2/monolayer-$MoTe_2$ van der Waals heterostructure. By stacking MoS_2/$MoTe_2$ on graphene, we fabricated a broadband photodetector that exhibited a high photoresponsivity (>100 mA/W) and a low dark current (60 nA) over a wide wavelength range (488–1550 nm).

Keywords: 2D materials; photodetectors; van der Waals heterostructure

check for updates

Citation: Park, D.-H.; Lee, H.C. Photogating Effect of Atomically Thin Graphene/MoS_2/$MoTe_2$ van der Waals Heterostructures. *Micromachines* **2023**, *14*, 140. https://doi.org/10.3390/mi14010140

Academic Editor: Yongmin Jeon

Received: 31 October 2022
Revised: 30 December 2022
Accepted: 2 January 2023
Published: 4 January 2023

1. Introduction

Since the first report of the exfoliation of monolayer graphene [1], many two-dimensional (2D) materials, such as hexagonal boron nitride (hBN) [2], black phosphorous [3], and transition metal chalcogenides, including molybdenum disulfide (MoS_2) [4] and molybdenum ditelluride ($MoTe_2$), have been discovered [5,6]. Various optoelectronic devices, such as optical modulators, photovoltaics, waveguides, light-emitting diodes, and photodetectors, have been fabricated using these 2D materials [7–14]. In particular, significant efforts have been made to fabricate short-wave infrared (SWIR) photodetectors using graphene and other 2D materials [15–25]. These devices are widely used for biological imaging, remote sensing, night vision, and telecommunications, and the use of 2D materials eliminates the need to cool these devices to cryogenic temperatures. To this end, several van der Waals (vdW) heterostructures of 2D materials have been proposed, wherein the 2D materials are held together by vdW forces. Among the most promising vdW heterostructures of 2D materials are those that exhibit type−II band alignment owing to interlayer optical excitation, which allows for infrared absorption even if the bandgaps of the components are too large to allow them to absorb infrared light [26]. Moreover, type-II band alignment promotes charge separation at the interface, which is essential for photodetection [27]. It has recently been demonstrated that a monolayer-MoS_2/monolayer-$MoTe_2$ vdW heterostructure showed a distinct photovoltaic current in the infrared region at room temperature (1550 nm) [28]. However, this photodiode suffered from low photoresponsivity (<0.02 mA/W).

In this study, we investigated the modulation of the charge-carrier density of graphene in a vertical graphene/MoS_2/$MoTe_2$ vdW heterostructure. We fabricated a broadband graphene/MoS_2 photodetector with a MoS_2/$MoTe_2$ vdW heterostructure as the gate stack. We found that the graphene was significantly doped by the photoexcited charge generated in the MoS_2/$MoTe_2$ heterostructure and that type−II band alignment between MoS_2 and $MoTe_2$ resulted in a photoresponsivity greater than 100 mA/W with a dark current of 60 nA over a wide wavelength range. Thus, we were able to realize a SWIR graphene photodetector with high photoresponsivity.

2. Results and Discussion

Figure 1a shows a schematic of the process for fabricating the photodetector. After monolayer graphene was exfoliated and placed on a wafer substrate, monolayer MoS_2 was transferred onto the graphene layer using the PMMA transfer method, such that it partially covered the graphene. The overlapping graphene/MoS_2 region formed the Schottky junction of the device. Next, monolayer $MoTe_2$ was transferred onto the graphene/MoS_2 junction. To passivate the Schottky junction region, we covered it with a thick hBN layer. The vdW heterostructures were then annealed in a vacuum. Finally, we deposited a source electrode on the graphene layer and a drain electrode on the MoS_2 layer using e−beam lithography. The source and drain electrodes were neither connected to the $MoTe_2$ layer nor to the hBN layer. Therefore, the device was a graphene/MoS_2 Schottky diode in which the $MoTe_2$/hBN layer was stacked on the Schottky junction.

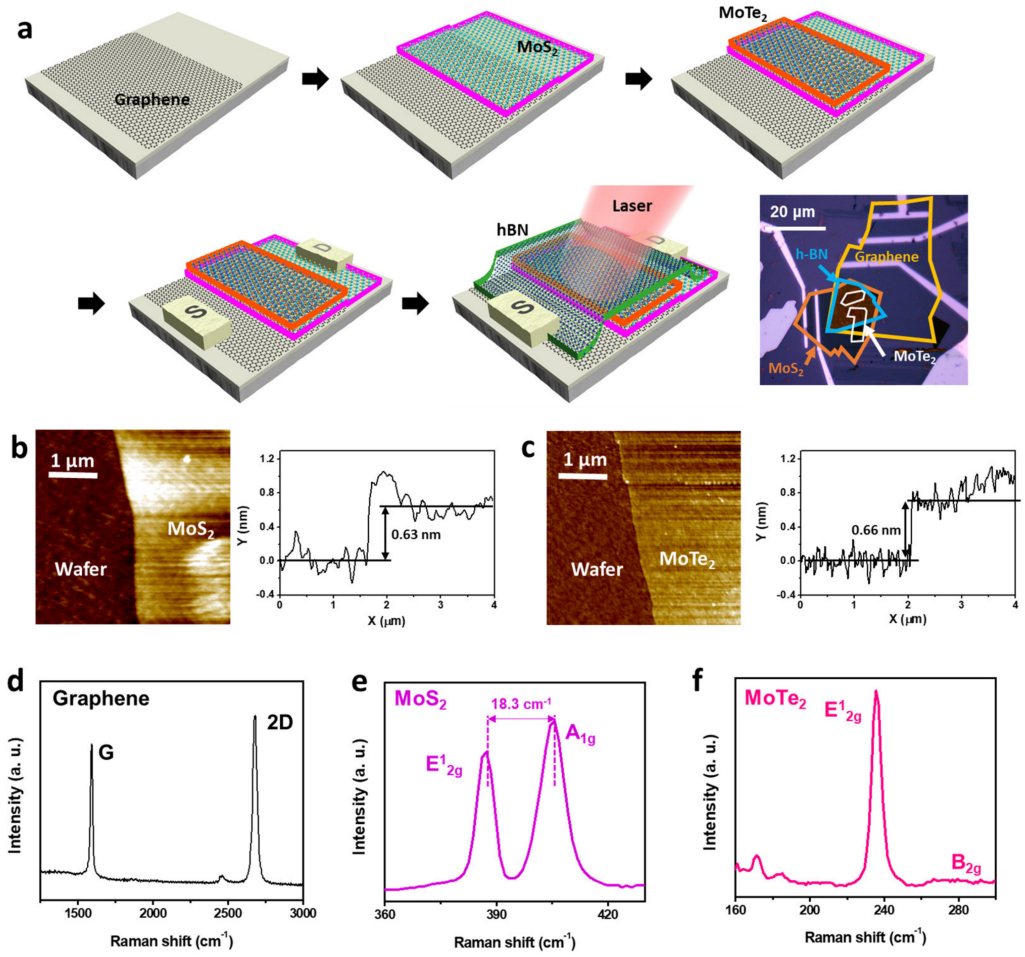

Figure 1. (**a**), Process for fabricating graphene/MoS_2/$MoTe_2$ photodetector. (**b**), AFM images (**left**) and corresponding cross−sectional height profiles (**right**) of standalone MoS_2 layer and (**c**), $MoTe_2$ layer used in photodetector. Raman spectra of (**d**), graphene, (**e**), MoS_2, and (**f**), $MoTe_2$.

Figure 1b,c show atomic force microscopy (AFM) images of the MoS_2 and $MoTe_2$ monolayers on the Si/SiO_2 wafer used to fabricate the photodetector. The height of the MoS_2 layer was 0.63 nm and that of the $MoTe_2$ layer was 0.66 nm; this confirmed that the MoS_2 and $MoTe_2$ structures were monolayers. To further assess the thicknesses of the graphene, MoS_2, and $MoTe_2$ layers, we determined their Raman spectra before they were transferred (Figure 1d, 532 nm). The ratio of the intensity of the 2D peak (Pos(2D) = 2682 cm^{-1}) of graphene to that of its G peak (Pos(G) = 1592 cm^{-1}) was slightly larger than 1. The height of the graphene layer was smaller than 1 nm, which indicated that the graphene layer was a monolayer (see Figure S1) [29]. In addition, the D peak of graphene

conventionally observed at approximately 1350 cm^{-1}, whose intensity is proportional to the defect density of graphene, was not present [30]. The two peaks of MoS_2 seen at 387.4 and 405.7 cm^{-1} were the E^1_{2g} and A_{1g} peaks, respectively. The distance between these two peaks is indicative of the number of MoS_2 layers, and it increases as the number of MoS_2 layers increases [31]. In this study, this distance was ~18 cm^{-1}, which confirmed that the MoS_2 layer was also a monolayer (Figure 1e). Figure 1f shows the Raman spectrum of the $MoTe_2$ layer. Only one distinctive peak was present at approximately 240 cm^{-1}. This was the E^1_{2g} peak of the $MoTe_2$. The absence of a peak at approximately 280 cm^{-1} (B_{2g}) indicated that this layer was also a monolayer [32].

Raman spectroscopy is a powerful tool, not only for the characterization of isolated 2D materials, but also for the vdW stacking of 2D materials, because the Raman active phonon modes of 2D materials are sensitive to changes in the degree of doping and strain of the materials, as well as their vdW interactions with other layers. To evaluate the quality of the vdW stacking at the Schottky junction, we performed a Raman spectroscopy analysis after fabricating the device, as is shown in Figure 1. First, we obtained the Raman intensity maps of the graphene G peak, MoS_2 A_{1g} peak, and $MoTe_2$ $E^1{}_{2g}$ peak, which allowed for the delineation of the edges of the graphene, MoS_2, and $MoTe_2$ layers with precision (Figure 2a). Because monolayered MoS_2 and $MoTe_2$ can be degraded by exposure to air, we focused on the MoS_2, graphene, graphene/MoS_2, and graphene/MoS_2/$MoTe_2$ regions that were passivated by hBN (Figure 2b). The integration time for one spot in the Raman image was 130 ms, which was sufficiently long for the photoexcited charge carriers in one material to transfer to the other materials. Figure 2c,d show the positions of the MoS_2 $E^1{}_{2g}$ (Pos($E^1{}_{2g}$)) and A_{1g} (Pos(A_{1g})) peaks, respectively. The Raman maps clearly show that the differences in Pos($E^1{}_{2g}$) and Pos(A_{1g}) depended on the stacking. Pos($E^1{}_{2g}$) and Pos(A_{1g}) were 387.2 and 405.5 cm^{-1}, respectively, in the case of the MoS_2 region; these values were similar to those for MoS_2 before the transfer process. On the other hand, in the region where MoS_2 was stacked on graphene, Pos(A_{1g}) was blue−shifted by 2 cm^{-1}, while Pos($E^1{}_{2g}$) remained the same (Figure 2e). Thus, Pos($E^1{}_{2g}$) and Pos(A_{1g}) could be changed by changing the degree of doping [33], strain [34], and vdW interactions with the neighboring materials [35]. However, a shift in the A_{1g} peak of the MoS_2 by 1 cm^{-1} would require the removal of electrons in a density of 1×10^{13}. In addition, the biaxial strain in MoS_2 changes both Pos($E^1{}_{2g}$) and Pos(A_{1g}), which was not the case in this study. Therefore, we attributed the blue−shift of the Pos(A_{1g}) to the stiffening of the A_{1g} phonon by the graphene−MoS_2 vdW interaction [35]. This was indicative of interlayer coupling between graphene and MoS_2. For graphene/MoS_2/$MoTe_2$, the $E^1{}_{2g}$ and A_{1g} peaks were red-shifted by ~3 and ~2 cm^{-1}, respectively, from those of graphene/MoS_2, which was consistent with previous reports [36]. We believe that the red-shifting of the peaks was attributable to the tensile strain or the relaxation of the compressive strain owing to the mismatch in the lattice constants of the MoS_2 (0.316 nm) and $MoTe_2$ (0.352 nm).

We also monitored Pos(G) (Figure 2f) and Pos(2D) (Figure 2g) for graphene. Because Pos(G) and Pos(2D) are highly sensitive to the strain and doping level of graphene, these factors can be estimated from the peak positions (Figure 2h) [37]. Pos(G) and Pos(2D) for the graphene−only region were 1585.7 and 2671.5 cm^{-1}, respectively; these values correspond to a tensile strain of ~0.05% and hole doping level of ~6×10^{12} cm^{-2}. However, in the graphene/MoS_2 region, the G and 2D peaks were both blue-shifted compared with those in the graphene-only region, which indicated that interlayer coupling with MoS_2 induced a compressive strain of 0.1% and the electron doping of graphene at the ~3×10^{12} cm^{-2} level. The compressive strain induced in graphene by MoS_2 also suggests that the graphene/MoS_2 heterostructure was well formed in the analyzed area [38]. The electron doping of graphene implies that electrons were transferred from MoS_2 to graphene. After $MoTe_2$ was stacked on graphene, the compressive strain in graphene was relaxed slightly, probably because of the tensile strain generated or the relaxation of the MoS_2−induced compressive strain by $MoTe_2$. In addition, the graphene became less hole-doped compared with the graphene/MoS_2 region, which meant that the stacking

of $MoTe_2$ enhanced the transfer of electrons to graphene. The underlying mechanism of graphene doping under the different heterostructures is discussed in more detail later in this paper.

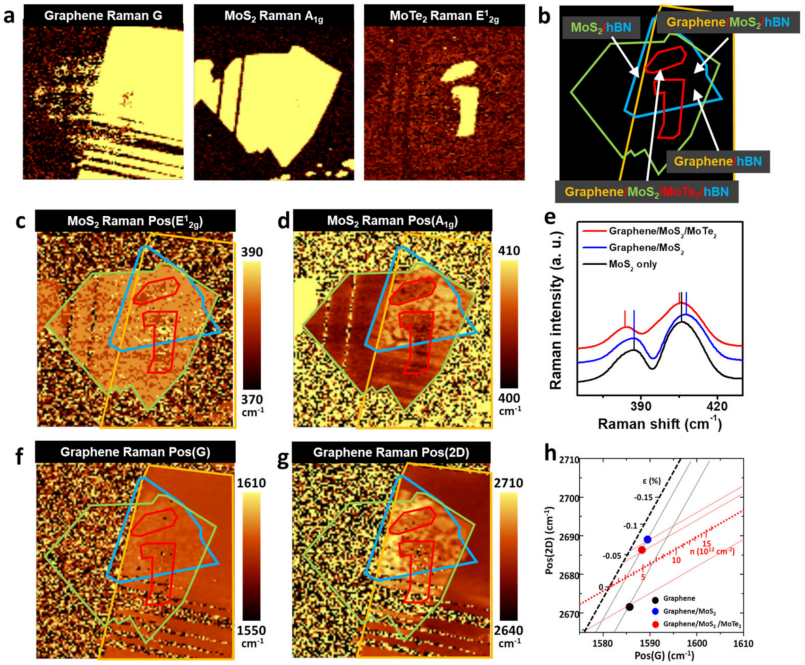

Figure 2. (**a**), Raman intensity maps of G peak of graphene (**left**), A_{1g} peak of MoS_2 (**middle**), and $E^1{}_{2g}$ peak of $MoTe_2$ (**right**). (**b**), Locations of graphene (orange), MoS_2 (green), $MoTe_2$ (red), and hBN (blue) as determined using Raman spectroscopy and optical microscopy. (**c**), Pos($E^1{}_{2g}$) and (**d**), Pos(A_{1g}) maps of MoS_2 layer. (**e**), Raman spectra of MoS_2 in MoS2-only region (black), graphene/MoS_2 region (blue), and graphene/MoS_2/$MoTe_2$ region (red). (**f**), Pos(G) and (**g**), Pos(2D) maps of graphene. (**h**), Average Pos(G) and Pos(2D) values in Raman spectra of graphene in graphene-only region (black), graphene/MoS_2 region (blue), and graphene/MoS_2/$MoTe_2$ region (red).

To investigate the charge transfer at the graphene/MoS_2 and MoS_2/$MoTe_2$ interfaces, we performed photoluminescence (PL) spectroscopy (Figure 3). The PL spectrum of monolayered MoS_2 originates from the radiative recombination of three types of quasiparticles: A excitons (~1.85 eV), B excitons (~2.03 eV), and A− trions (~1.80 eV) [39]. Figure 3a shows the band diagrams of the three quasiparticles. The relative contributions of the A excitons and A− trions to the PL spectrum of MoS_2 depend on the Fermi level of MoS_2 [40]. When MoS_2 is hole-doped or less electron-doped, the PL peak from the A excitons is very strong compared with that of the A− trions. On the other hand, the A exciton peak decreases as MoS_2 becomes n-doped, because an excessive number of electrons in MoS_2 bind to the photoexcited electron-hole pairs to form trions.

Figure 3b,c show the total PL intensity and position of the A peak (A exciton + A− trion, respectively). The efficient PL quenching of graphene differentiates the graphene/MoS_2/$MoTe_2$ region from the MoS_2/$MoTe_2$ region. The $MoTe_2$ PL peak at approximately 1 eV was not observed, thus confirming that efficient charge separation had occurred between MoS_2 and $MoTe_2$ (Figure 3d).

To further investigate charge transfer at the interfaces, we analyzed the PL spectra of the MoS2-only (Figure 3e), graphene/MoS_2 (Figure 3f), and graphene/MoS_2/$MoTe_2$ (Figure 3g) regions in the 1.70–2.05 eV range. The PL spectrum of the MoS2-only region exhibited A exciton, B exciton, and A− trion PL peaks (Figure 3e). Specifically, the A− trion peak was stronger than the A exciton peak, which was in keeping with the fact that MoS_2 is an n-type semiconductor. The PL spectrum of MoS_2 changed when it was placed over graphene. In this case, the exciton PL peak was stronger than the

A− trion peak. This means that the photoexcited electrons in MoS_2 were transferred to graphene, while the photoexcited holes were accumulated in MoS_2. This charge transfer can inhibit the radiative recombination of A− trions in MoS_2 by spatially separating the photogenerated electrons and holes. In addition, it simultaneously induced the electron doping of graphene during the optical measurements. This was consistent with the Raman spectroscopy analysis, which showed that the formation of the graphene/MoS_2 structure resulted in the n-type doping of graphene (Figure 2h). The work function of the MoS_2 was larger than that of graphene [41]. Thus, the electrons in the graphene were transferred to the MoS_2 layer after contact, resulting in an electric field whose direction was toward MoS_2 at the graphene/MoS_2 interface, as is shown in Figure 3h. Therefore, the photogenerated electrons in MoS_2 could be easily transferred to graphene.

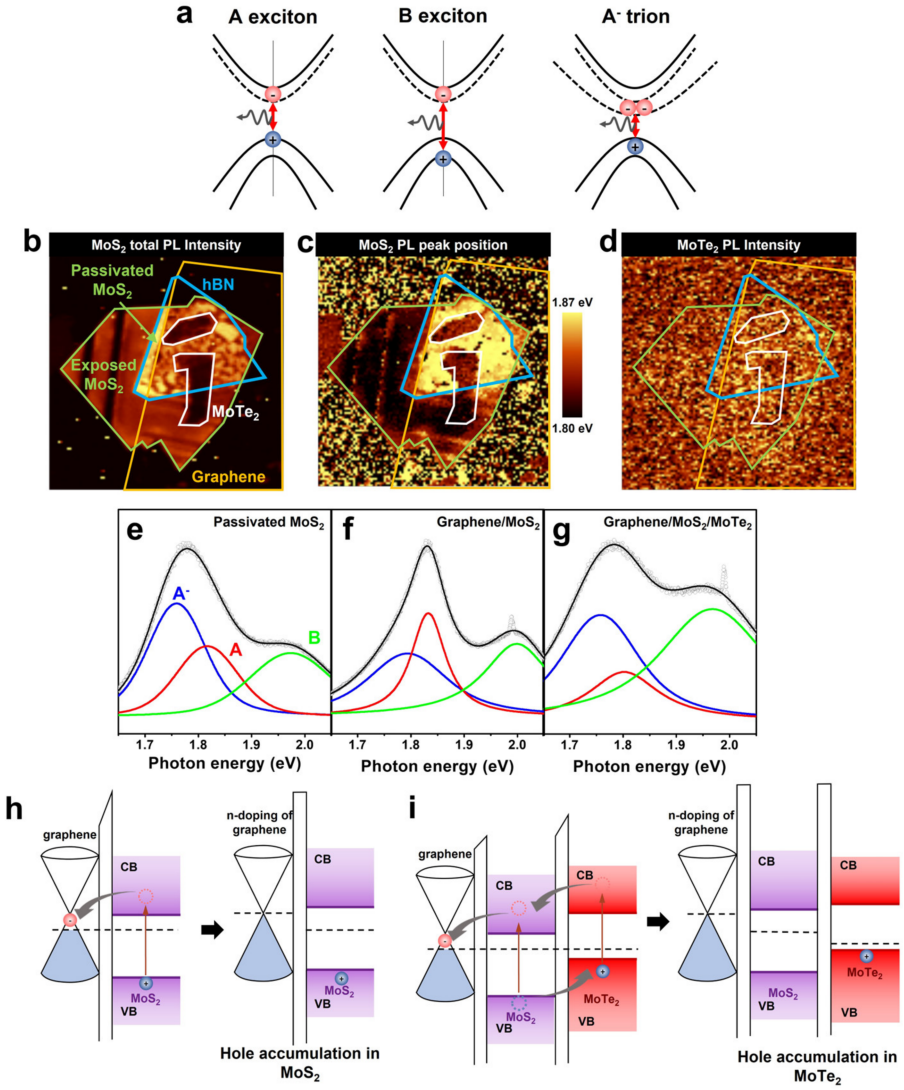

Figure 3. (**a**), Schematics showing A exciton (**left**), B exciton (**middle**), and A− trion (**right**) in MoS_2. (**b**), MoS_2 PL intensity map and (**c**), PL peak position map. (**d**), $MoTe_2$ PL intensity map. (**e**), PL spectra of MoS_2 in MoS2-only region (passivated by hBN), (**f**), graphene/MoS_2 region, and (**g**), graphene/MoS_2/$MoTe_2$ region. (**h**), Energy band diagrams of graphene/MoS_2, and (**i**), graphene/MoS_2/$MoTe_2$ before (**left**) and under illumination (**right**).

In the region where $MoTe_2$ was stacked on the graphene/MoS_2 structure, resulting in graphene/MoS_2/$MoTe_2$, the A exciton peak was not observed. This implies that holes did not accumulate in the MoS_2 layer in the resulting structure. This can be explained by the fact that MoS_2 and $MoTe_2$ exhibited type-II band alignment (Figure 3i) and that

the photogenerated holes (electrons) in MoS_2 ($MoTe_2$) were transferred to $MoTe_2$ (MoS_2). The transfer of holes from MoS_2 to $MoTe_2$ aided the separation of the photoexcited electrons and holes in graphene, resulting in efficient PL quenching (Figure 3b). The type−II band alignment between MoS_2 and $MoTe_2$ also explains the increased electron doping of graphene in graphene/MoS_2/$MoTe_2$ after the stacking of $MoTe_2$ on graphene/MoS_2, as per the Raman spectroscopy analysis (Figure 2h). The photoexcited holes trapped in $MoTe_2$ could enter graphene through MoS_2, resulting in the additional electron doping of graphene. This is because the MoS_2 layer was too thin to screen for holes in $MoTe_2$.

Figure 4a shows the current-voltage (I–V) characteristics of the photodetector under continuous illumination with a 50 nW light over the graphene/MoS_2/$MoTe_2$ region. The laser spot was placed away from the metal electrodes to exclude the photocurrent from the graphene/metal and MoS_2/metal junctions. In the dark, the I–V characteristics were similar to those of a typical Schottky diode with series resistances (Figure S2). The series resistances can be attributed to the resistances of the graphene and MoS_2 layers and the contact resistances between graphene, MoS_2 layers, and the metal electrodes. The current increased under illumination, whose wavelength range was 488–1550 nm. A finite photocurrent was observed at zero voltage, showing the photovoltaic effect of the device [42]. However, the photocurrent was almost absent at zero voltage and increased as V was increased. It implies that the photocurrent mainly originated from the photogating effect rather than the photovoltaic effect.

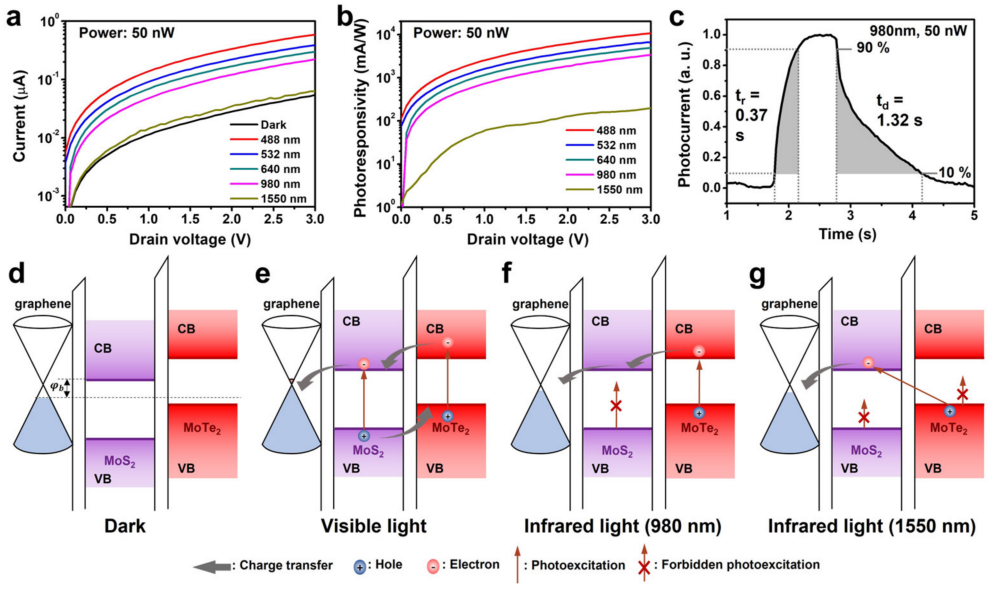

Figure 4. (**a**), Current-voltage curves of photodetector under illumination with 50 nW laser and (**b**), corresponding photoresponsivity-voltage curves. (**c**), Time-resolved photocurrent of device under illumination with 50 nW laser at 980 nm. (**d**), Energy band diagram and charge-transfer processes in dark and under illumination with (**e**), visible laser, (**f**), infrared laser at 980 nm, and (**g**), infrared laser at 1550 nm.

For photodetectors based on 2D materials, the photoresponsivity, R, and specific detectivity, D^*, are generally used as the figures of merit [42]. R is the photocurrent per incident unit optical power, and D^* is a measure of the smallest detectable signal from the photodetector and is given by $D^* = RA^{1/2}/\overline{I_n^2}^{1/2}$, where A is the illumination area (1200 μm^2) and $\overline{I_n^2}^{1/2}$ is the root-mean-square noise current. The area of the whole photodetector was larger than the laser spot size. Figure 4b shows the estimated R value as a function of V for various wavelengths. The device exhibited the maximum R value at V = 3 V; however, R increased when we applied a higher V. For instance, R exceeded 10^4 mA/W at 488 nm and 10^2 mA/W at all the other wavelengths. Notably, R was 3×10^3

and 1.8×10^2 mA/W at 980 and 1550 nm, respectively; these are the wavelengths at which MoS_2 is optically inactive. When the noise current is dominated by shot noise, D^* can be estimated using the following equation [43]:

$$D^* = RA^{1/2}/(2eI_{dark})^{1/2} \quad (1)$$

D^* was estimated to be 3×10^{11}, 9×10^{10}, and 5×10^9 Jones at 488, 980, and 1550 nm, respectively. Figure 4c shows the time-resolved photocurrent of the device under illumination with a 980 nm light at V = 3 V. The rise and decay times were 0.37 and 1.32 s, respectively (see also Table S1 [15,22,24,44–49]).

In the present study, the photogating effect was a photoinduced change in the Fermi level of the material in question, namely, the graphene under MoS_2. Under the photogating effect, the value of φ_b at the graphene/MoS_2 junction was modulated by light, which, in turn, changed the device current. The photogating of the graphene-neighboring MoS_2 layer was well known (Figure 4d,e) [50]. The MoS_2 layer absorbed light, resulting in the photoexcitation of electrons and holes. Owing to the electric field at the graphene/MoS_2 interface and the difference in the energies of the conduction band edge of MoS_2 and the Fermi level of graphene, the photoexcited electrons were transferred from MoS_2 to graphene. Meanwhile, the photoexcited holes of MoS_2 were transferred to $MoTe_2$, where they were trapped. This altered the electric field near the MoS_2 layer, causing the n-doping of graphene. Consequently, φ_b decreased under illumination, resulting in a reduction in the Schottky barrier height between graphene and MoS_2. Although this explains the photoresponse of the device under visible light, the photocurrent under infrared light (980 and 1550 nm) requires an additional explanation, because monolayered MoS_2 cannot absorb light with wavelengths larger than 800 nm. Considering the $MoTe_2$ monolayer, we propose the following mechanism to explain the photoresponse of the device under infrared light. When illuminated with 980 nm light (Figure 4f), $MoTe_2$ absorbs the light, generating photoexcited electrons and holes. These photoexcited electrons tunnel toward graphene directly or through the MoS_2 layer, while the photoexcited holes remain in $MoTe_2$. This leads to the n-doping of graphene, resulting in a photocurrent in the device. In the case of 1550 nm light (Figure 4g), both MoS_2 and monolayered $MoTe_2$ are optically inactive when they are separated. However, because monolayered MoS_2 and monolayered $MoTe_2$ exhibit type−II band alignment, an interlayer transition occurs between them when they are stacked. The photoexcited electrons in MoS_2 and holes in $MoTe_2$ are separated by the transfer of electrons to graphene or the extraction of electrons owing to the drain bias. The remaining holes in $MoTe_2$ cause the n−doping of graphene, thus reducing φ_b at the graphene/MoS_2 junction.

To confirm the role of the $MoTe_2$ layer, we fabricated a graphene/MoS_2 Schottky diode without a $MoTe_2$ layer on the Schottky junction and measured its photoresponse. As shown in Figure S3a, the current of the device barely changed under infrared light (980 and 1550 nm). Time-resolved current measurements were performed under infrared light illumination (Figure S3b). However, no change in the current was observed during the measurements. The absence of a photoresponse excludes the possibility that the detrapping of charge carriers near the graphene/MoS_2 interface was responsible for the photoresponse under infrared light. Thus, these results clearly indicate that the absorption of infrared light by graphene did not contribute to the photocurrent of the device and that monolayered MoS_2 alone did not induce the photogating of graphene under infrared light. It is well known that photogenerated charge carriers recombine within a few picoseconds because of plasmon emission and carrier-phonon scattering [51]. Consequently, the photogenerated charge carriers in graphene were annihilated before the charges at the graphene/MoS_2 interface were separated. In addition, the bandgap of MoS_2 inhibits the absorption of infrared light, making the graphene/MoS_2 junction inactive under infrared light illumination. In summary, the observed photoresponse of the photodetector shown in Figure 4 was attributable to the $MoTe_2$ layer deposited on the MoS_2/graphene Schottky junction.

In conclusion, we realized a graphene/MoS_2 barristor-based photodetector that exploited the photogating of graphene based on the type−II band alignment in the monolayered MoS_2/monolayered $MoTe_2$ structure. The device showed a photoresponsivity as high as 10^4 mA/W and a detectivity of 3×10^{11} Jones under visible light. More importantly, we were able to simultaneously achieve a photoresponsivity of more than 10^2 mA/W and detectivity of more than 5×10^9 Jones in the 980–1550 nm range.

Supplementary Materials: The following supporting information can be downloaded at: https://www.mdpi.com/article/10.3390/mi14010140/s1, Figure S1: AFM image (left) and corresponding cross-sectional height profile (right) of graphene used in the photodetector; Figure S2: Dark current-voltage characteristics of the photodetector; Figure S3: a, Current–voltage curves of graphene/MoS2 photodetector without MoTe2 layer under illumination with 1-μW laser and b, time-resolved photocurrent of device under illumination with 1-μW laser at 980 nm; Table S1: Comparison of the performance parameters for photodetectors.

Author Contributions: Experimental data acquisition, writing—original draft preparation, D.-H.P.; Conceptualization, writing—review and editing, supervision, H.C.L. All authors have read and agreed to the published version of the manuscript.

Funding: This work was supported by the National Research Foundation of Korea (NRF) grant funded by the Korea government (MSIT) (No. 2022R1C1C1013173).

Institutional Review Board Statement: Not applicable.

Informed Consent Statement: Not applicable.

Data Availability Statement: Not applicable.

Acknowledgments: This work was supported by the National Research Foundation of Korea (NRF) grant funded by the Korea government (MSIT) (No. 2022R1C1C1013173).

Conflicts of Interest: The authors declare no conflict of interest.

References

1. Novoselov, K.S.; Geim, A.K.; Morozov, S.V.; Jiang, D.-E.; Zhang, Y.; Dubonos, S.V.; Grigorieva, I.V.; Firsov, A.A. Electric field effect in atomically thin carbon films. *Science* **2004**, *306*, 666–669. [CrossRef]
2. Pacile, D.; Meyer, J.; Girit, Ç.; Zettl, A. The two-dimensional phase of boron nitride: Few-atomic-layer sheets and suspended membranes. *Appl. Phys. Lett.* **2008**, *92*, 133107. [CrossRef]
3. Ling, X.; Wang, H.; Huang, S.; Xia, F.; Dresselhaus, M.S. The renaissance of black phosphorus. *Proc. Natl. Acad. Sci. USA* **2015**, *112*, 4523–4530. [CrossRef]
4. Mak, K.F.; Lee, C.; Hone, J.; Shan, J.; Heinz, T.F. Atomically thin MoS_2: A new direct-gap semiconductor. *Phys. Rev. Lett.* **2010**, *105*, 136805. [CrossRef]
5. Wang, Y.; Xiao, J.; Zhu, H.; Li, Y.; Alsaid, Y.; Fong, K.Y.; Zhou, Y.; Wang, S.; Shi, W.; Wang, Y. Structural phase transition in monolayer $MoTe_2$ driven by electrostatic doping. *Nature* **2017**, *550*, 487–491. [CrossRef]
6. Cho, S.; Kim, S.; Kim, J.H.; Zhao, J.; Seok, J.; Keum, D.H.; Baik, J.; Choe, D.-H.; Chang, K.J.; Suenaga, K. Phase patterning for ohmic homojunction contact in $MoTe_2$. *Science* **2015**, *349*, 625–628. [CrossRef]
7. Lopez-Sanchez, O.; Lembke, D.; Kayci, M.; Radenovic, A.; Kis, A. Ultrasensitive photodetectors based on monolayer MoS_2. *Nat. Nanotechnol.* **2013**, *8*, 497–501. [CrossRef]
8. Zhou, X.; Hu, X.; Yu, J.; Liu, S.; Shu, Z.; Zhang, Q.; Li, H.; Ma, Y.; Xu, H.; Zhai, T. 2D layered material-based van der Waals heterostructures for optoelectronics. *Adv. Funct. Mater.* **2018**, *28*, 1706587. [CrossRef]
9. Britnell, L.; Ribeiro, R.M.; Eckmann, A.; Jalil, R.; Belle, B.D.; Mishchenko, A.; Kim, Y.-J.; Gorbachev, R.V.; Georgiou, T.; Morozov, S.V. Strong light-matter interactions in heterostructures of atomically thin films. *Science* **2013**, *340*, 1311–1314. [CrossRef]
10. Clark, G.; Schaibley, J.R.; Ross, J.; Taniguchi, T.; Watanabe, K.; Hendrickson, J.R.; Mou, S.; Yao, W.; Xu, X. Single defect light-emitting diode in a van der Waals heterostructure. *Nano Lett.* **2016**, *16*, 3944–3948. [CrossRef]
11. Lee, C.-H.; Lee, G.-H.; Van Der Zande, A.M.; Chen, W.; Li, Y.; Han, M.; Cui, X.; Arefe, G.; Nuckolls, C.; Heinz, T.F. Atomically thin p–n junctions with van der Waals heterointerfaces. *Nat. Nanotechnol.* **2014**, *9*, 676–681. [CrossRef]
12. Ross, J.S.; Rivera, P.; Schaibley, J.; Lee-Wong, E.; Yu, H.; Taniguchi, T.; Watanabe, K.; Yan, J.; Mandrus, D.; Cobden, D. Interlayer exciton optoelectronics in a 2D heterostructure p–n junction. *Nano Lett.* **2017**, *17*, 638–643. [CrossRef]
13. Wang, F.; Wang, Z.; Xu, K.; Wang, F.; Wang, Q.; Huang, Y.; Yin, L.; He, J. Tunable GaTe-MoS_2 van der Waals p–n junctions with novel optoelectronic performance. *Nano Lett.* **2015**, *15*, 7558–7566. [CrossRef]

14. Yu, W.J.; Vu, Q.A.; Oh, H.; Nam, H.G.; Zhou, H.; Cha, S.; Kim, J.-Y.; Carvalho, A.; Jeong, M.; Choi, H. Unusually efficient photocurrent extraction in monolayer van der Waals heterostructure by tunnelling through discretized barriers. *Nat. Commun.* **2016**, *7*, 13278. [CrossRef] [PubMed]
15. Yu, W.; Li, S.; Zhang, Y.; Ma, W.; Sun, T.; Yuan, J.; Fu, K.; Bao, Q. Near-infrared photodetectors based on $MoTe_2$/graphene heterostructure with high responsivity and flexibility. *Small* **2017**, *13*, 1700268. [CrossRef]
16. Ding, Y.; Zhou, N.; Gan, L.; Yan, X.; Wu, R.; Abidi, I.H.; Waleed, A.; Pan, J.; Ou, X.; Zhang, Q. Stacking-mode confined growth of 2H-$MoTe_2$/MoS_2 bilayer heterostructures for UV–vis–IR photodetectors. *Nano Energy* **2018**, *49*, 200–208. [CrossRef]
17. Huang, H.; Wang, J.; Hu, W.; Liao, L.; Wang, P.; Wang, X.; Gong, F.; Chen, Y.; Wu, G.; Luo, W. Highly sensitive visible to infrared $MoTe_2$ photodetectors enhanced by the photogating effect. *Nanotechnology* **2016**, *27*, 445201. [CrossRef]
18. Liu, Y.; Wang, F.; Wang, X.; Wang, X.; Flahaut, E.; Liu, X.; Li, Y.; Wang, X.; Xu, Y.; Shi, Y. Planar carbon nanotube–graphene hybrid films for high-performance broadband photodetectors. *Nat. Commun.* **2015**, *6*, 8589. [CrossRef] [PubMed]
19. Yang, F.; Cong, H.; Yu, K.; Zhou, L.; Wang, N.; Liu, Z.; Li, C.; Wang, Q.; Cheng, B. Ultrathin broadband germanium–graphene hybrid photodetector with high performance. *ACS Appl. Mater. Interfaces* **2017**, *9*, 13422–13429. [CrossRef]
20. Jain, S.K.; Low, M.X.; Taylor, P.D.; Tawfik, S.A.; Spencer, M.J.; Kuriakose, S.; Arash, A.; Xu, C.; Sriram, S.; Gupta, G. 2D/3D Hybrid of MoS_2/GaN for a High-Performance Broadband Photodetector. *ACS Appl. Electron. Mater.* **2021**, *3*, 2407–2414. [CrossRef]
21. Gomathi, P.T.; Sahatiya, P.; Badhulika, S. Large-area, flexible broadband photodetector based on ZnS–MoS_2 hybrid on paper substrate. *Adv. Funct. Mater.* **2017**, *27*, 1701611. [CrossRef]
22. Zhang, K.; Fang, X.; Wang, Y.; Wan, Y.; Song, Q.; Zhai, W.; Li, Y.; Ran, G.; Ye, Y.; Dai, L. Ultrasensitive near-infrared photodetectors based on a graphene–$MoTe_2$–graphene vertical van der Waals heterostructure. *ACS Appl. Mater. Interfaces* **2017**, *9*, 5392–5398. [CrossRef]
23. Chang, K.E.; Kim, C.; Yoo, T.J.; Kwon, M.G.; Heo, S.; Kim, S.Y.; Hyun, Y.; Yoo, J.I.; Ko, H.C.; Lee, B.H. High-responsivity near-infrared photodetector using gate-modulated graphene/germanium Schottky junction. *Adv. Electron. Mater.* **2019**, *5*, 1800957. [CrossRef]
24. Ye, L.; Li, H.; Chen, Z.; Xu, J. Near-infrared photodetector based on MoS_2/black phosphorus heterojunction. *ACS Photonics* **2016**, *3*, 692–699. [CrossRef]
25. Wang, L.; Jie, J.; Shao, Z.; Zhang, Q.; Zhang, X.; Wang, Y.; Sun, Z.; Lee, S.T. MoS_2/Si heterojunction with vertically standing layered structure for ultrafast, high-detectivity, self-driven visible–near infrared photodetectors. *Adv. Funct. Mater.* **2015**, *25*, 2910–2919. [CrossRef]
26. Qi, T.; Gong, Y.; Li, A.; Ma, X.; Wang, P.; Huang, R.; Liu, C.; Sakidja, R.; Wu, J.Z.; Chen, R. Interlayer transition in a vdW heterostructure toward ultrahigh detectivity shortwave infrared photodetectors. *Adv. Funct. Mater.* **2020**, *30*, 1905687. [CrossRef]
27. Gong, Y.; Lin, J.; Wang, X.; Shi, G.; Lei, S.; Lin, Z.; Zou, X.; Ye, G.; Vajtai, R.; Yakobson, B.I. Vertical and in-plane heterostructures from WS_2/MoS_2 monolayers. *Nat. Mater.* **2014**, *13*, 1135–1142. [CrossRef]
28. Zhang, K.; Zhang, T.; Cheng, G.; Li, T.; Wang, S.; Wei, W.; Zhou, X.; Yu, W.; Sun, Y.; Wang, P. Interlayer transition and infrared photodetection in atomically thin type-II $MoTe_2$/MoS_2 van der Waals heterostructures. *ACS Nano* **2016**, *10*, 3852–3858. [CrossRef]
29. Ferrari, A.C.; Basko, D.M. Raman spectroscopy as a versatile tool for studying the properties of graphene. *Nat. Nanotechnol.* **2013**, *8*, 235–246. [CrossRef]
30. Eckmann, A.; Felten, A.; Mishchenko, A.; Britnell, L.; Krupke, R.; Novoselov, K.S.; Casiraghi, C. Probing the nature of defects in graphene by Raman spectroscopy. *Nano Lett.* **2012**, *12*, 3925–3930. [CrossRef]
31. Li, H.; Zhang, Q.; Yap, C.C.R.; Tay, B.K.; Edwin, T.H.T.; Olivier, A.; Baillargeat, D. From bulk to monolayer MoS_2: Evolution of Raman scattering. *Adv. Funct. Mater.* **2012**, *22*, 1385–1390. [CrossRef]
32. Ruppert, C.; Aslan, B.; Heinz, T.F. Optical properties and band gap of single-and few-layer $MoTe_2$ crystals. *Nano Lett.* **2014**, *14*, 6231–6236. [CrossRef] [PubMed]
33. Chakraborty, B.; Bera, A.; Muthu, D.; Bhowmick, S.; Waghmare, U.V.; Sood, A. Symmetry-dependent phonon renormalization in monolayer MoS_2 transistor. *Phys. Rev. B* **2012**, *85*, 161403. [CrossRef]
34. Rice, C.; Young, R.; Zan, R.; Bangert, U.; Wolverson, D.; Georgiou, T.; Jalil, R.; Novoselov, K. Raman-scattering measurements and first-principles calculations of strain-induced phonon shifts in monolayer MoS_2. *Phys. Rev. B* **2013**, *87*, 081307. [CrossRef]
35. Zhou, K.-G.; Withers, F.; Cao, Y.; Hu, S.; Yu, G.; Casiraghi, C. Raman modes of MoS2 used as fingerprint of van der Waals interactions in 2-D crystal-based heterostructures. *ACS Nano* **2014**, *8*, 9914–9924. [CrossRef]
36. Duong, N.T.; Lee, J.; Bang, S.; Park, C.; Lim, S.C.; Jeong, M.S. Modulating the functions of MoS_2/$MoTe_2$ van der Waals heterostructure via thickness variation. *ACS Nano* **2019**, *13*, 4478–4485. [CrossRef]
37. Lee, J.E.; Ahn, G.; Shim, J.; Lee, Y.S.; Ryu, S. Optical separation of mechanical strain from charge doping in graphene. *Nat. Commun.* **2012**, *3*, 1024. [CrossRef] [PubMed]
38. Li, X.; Yu, S.; Wu, S.; Wen, Y.; Zhou, S.; Zhu, Z. Structural and electronic properties of superlattice composed of graphene and monolayer MoS_2. *J. Phys. Chem. C* **2013**, *117*, 15347–15353. [CrossRef]
39. Mak, K.F.; He, K.; Lee, C.; Lee, G.H.; Hone, J.; Heinz, T.F.; Shan, J. Tightly bound trions in monolayer MoS_2. *Nat. Mater.* **2013**, *12*, 207–211. [CrossRef]
40. Mouri, S.; Miyauchi, Y.; Matsuda, K. Tunable photoluminescence of monolayer MoS_2 via chemical doping. *Nano Lett.* **2013**, *13*, 5944–5948. [CrossRef] [PubMed]

41. Schulman, D.S.; Arnold, A.J.; Das, S. Contact engineering for 2D materials and devices. *Chem. Soc. Rev.* **2018**, *47*, 3037–3058. [CrossRef] [PubMed]
42. Li, H.; Li, X.; Park, J.-H.; Tao, L.; Kim, K.K.; Lee, Y.H.; Xu, J.-B. Restoring the photovoltaic effect in graphene-based van der Waals heterojunctions towards self-powered high-detectivity photodetectors. *Nano Energy* **2019**, *57*, 214–221. [CrossRef]
43. Long, M.; Wang, P.; Fang, H.; Hu, W. Progress, challenges, and opportunities for 2D material based photodetectors. *Adv. Funct. Mater.* **2019**, *29*, 1803807. [CrossRef]
44. Wang, W.; Klots, A.; Prasai, D.; Yang, Y.; Bolotin, K.I.; Valentine, J. Hot electron-based near-infrared photodetection using bilayer MoS_2. *Nano Lett.* **2015**, *15*, 7440–7444. [CrossRef]
45. John, J.W.; Dhyani, V.; Maity, S.; Mukherjee, S.; Ray, S.K.; Kumar, V.; Das, S. Broadband infrared photodetector based on nanostructured $MoSe_2$–Si heterojunction extended up to 2.5 μm spectral range. *Nanotechnology* **2020**, *31*, 455208. [CrossRef]
46. Liu, C.-H.; Chang, Y.-C.; Norris, T.B.; Zhong, Z. Graphene photodetectors with ultra-broadband and high responsivity at room temperature. *Nat. Nanotechnol.* **2014**, *9*, 273–278. [CrossRef]
47. Engel, M.; Steiner, M.; Avouris, P. Black phosphorus photodetector for multispectral, high-resolution imaging. *Nano Lett.* **2014**, *14*, 6414–6417. [CrossRef]
48. Kumar, R.; Khan, M.A.; Anupama, A.; Krupanidhi, S.B.; Sahoo, B. Infrared photodetectors based on multiwalled carbon nanotubes: Insights into the effect of nitrogen doping. *Appl.Surf. Sci.* **2021**, *538*, 148187. [CrossRef]
49. Sefidmooye Azar, N.; Bullock, J.; Shrestha, V.R.; Balendhran, S.; Yan, W.; Kim, H.; Javey, A.; Crozier, K.B. Long-wave infrared photodetectors based on 2D platinum diselenide atop optical cavity substrates. *ACS Nano* **2021**, *15*, 6573–6581. [CrossRef]
50. De Fazio, D.; Goykhman, I.; Yoon, D.; Bruna, M.; Eiden, A.; Milana, S.; Sassi, U.; Barbone, M.; Dumcenco, D.; Marinov, K. High responsivity, large-area graphene/MoS_2 flexible photodetectors. *ACS Nano* **2016**, *10*, 8252–8262. [CrossRef] [PubMed]
51. Rana, F.; George, P.A.; Strait, J.H.; Dawlaty, J.; Shivaraman, S.; Chandrashekhar, M.; Spencer, M.G. Carrier recombination and generation rates for intravalley and intervalley phonon scattering in graphene. *Phys. Rev. B* **2009**, *79*, 115447. [CrossRef]